Transactions on Machine Intelligence 6(2) (2023) 89-103

ISSN Online: 2821-1693

Transactions on Machine Intelligence

Journal Homepage: https://tmachineintelligence.ir/index.php/TMI

An Improved Multiport Power Converter for Grid-tied PV-EV Charging Systems

A. Shalbaf [1,*]

[1] Department of Electrical Engineering, Shahid Chamran University, Ahvaz, Iran

ARTICLE INFO

Article History:
Received 6 March 2023
Received in revised form
3 May 2023
Accepted 18 June 2023
Available online 19 June 2023

Keywords:
Multiport Converter, Electric Vehicles (EV), Vehicle to Grid (V2G), Renewable Energy

ABSTRACT

Renewable energy is in high demand for residential use, and solar energy is a favored source due to its popularity. One of the benefits of incorporating solar energy into EV charging systems is the reduction of GHG emissions while also lessening the load on the electrical grid, thus aiding in grid stabilization during peak hours. Integrated power converter topologies between photovoltaic (PV) panels, grid, and EV provide improved efficiency and reduced size, weight, and cost compared to non-integrated structures. Nevertheless, conventional integrated topologies mainly rely on traditional sub-converters which experience high voltage stresses on the semiconductor devices and low voltage gains. The paper presents a novel Multiport Power Converter, which is integrated into grid-tied PV-EV charging systems. This Converter is capable of offering lowered voltage stress on the bidirectional EV-side converter, thus improving the system's efficiency. Additionally, it can achieve a higher voltage gain for the PV-side converter operations. The converter can function in various modes- grid to EV, EV to grid, PV/EV to grid, PV to EV, and PV to grid. To validate the proposed converter, a MATLAB-based simulation programme is utilised to verify the theoretical analysis and performance of the proposed converter.

1. INTRODUCTION

Electric vehicles and photovoltaic systems are two promising solutions for controlling greenhouse gas (GHG) emissions, which are a critical cause of environmental damage and global warming, as they limit the use of fossil fuels [1,2]. In recent years, electric vehicles have garnered significant attention, and the global EV market has reached a milestone of ten million vehicles, with a remarkable growth of 43% in 2020 [3]. However, EVs require a substantial amount of electrical power for charging, which can pose a significant challenge, particularly during the day. This can lead to an increased demand for the public power grid and peak load growth. To combat this issue, using green and renewable energy sources like photovoltaic and wind energy can be beneficial. In addition to the environmental benefits, electric vehicle charging systems that use both photovoltaic (PV) panels and the grid offer advantages for EV owners and utilities [4,5]. The PV panels generate power for charging EVs locally, reducing demand on the electric grid and resulting in significant cost savings. Additionally, vehicle-to-grid (V2G) and PV to

* Corresponding Author: ali.shalbaf96@gmail.com
Department of Electrical Engineering, Shahid Chamran University, Ahvaz, Iran

http://dx.doi.org/10.47176/TMI.2023.89

© 2023 by the authors. Licensee T.M.I, Tehran, Iran. This article is an open access article distributed under the terms and conditions of the Creative Commons Attribution (CC-BY) license (http://creativecommons.org/licenses/by/4.0/).

Grid (PV2G) technologies can support the electrical grid by utilizing the long parking time of EVs and reducing charging costs through selling power back to the grid [6-8].

Therefore, the integration of EV charging stations with renewable energies has been at the center of attention in recent years. The integrated topologies for charging EVs using PV and electrical Grid are categorized into isolated and non-isolated topologies [9-11]. Khan et al. [12] and Mouli et al. [13], proposed isolated integrated converters for EV charging stations for high-power applications. But they needed the multi-winding transformers in a tight package, which made the design and implementation process increasingly difficult, especially for high power flows. To remove multi-winding transformers, Bhattacharjee et al. [14], presented an isolated three-port converter with a two-winding transformer and a reduced number of active components. However, a large filter is necessary to minimize the current harmonics and also switching losses are not limited for integrated boost sub-converter. Another topology with a two-winding transformer is proposed by Khan et al. [15], which was able to be reconfigured into different topologies to operate in different modes. But the problem with this topology is the large number of semiconductor devices which can lead to a high switching loss.

Non-isolated structure, as another category of integrated topologies, can be simpler to design, since the multi-winding transformers, which are usually utilized in isolated topologies, can be removed in these converters. Saxena et al. [16], Monteiro et al. [17] and Verma et al. [18] reported the implementation of integrated non-isolated converters for charging stations using three converters connecting to a DC-link. However, they utilized the traditional boost, and bi-directional Buck-boost converters as PV-side and EV-side converters, respectively. These topologies provide a limited voltage gain, and the voltage stresses on the semiconductor devices are not limited. Verma et al. [19], removed the boost converter, and the PV panels were directly connected to the dc-bus. This could reduce one power conversion stage, but a high-voltage solar array is required for this structure.

To enhance traditional integrated converters, this paper proposes a multiport converter for EV charging stations that employs a switched-quasi-Z-source topology [20] to reduce voltage stress on the semiconductor devices utilized in the EV-side conversion stage. Lowering the voltage stress on the power switches can improve the converter's efficiency, and enables the selection of low-rated voltage semiconductor devices for the converter. Additionally, a Positive Output Super Lift Luo (POSL) topology is utilized instead of a conventional boost converter with limited voltage gain. This topology can be easily extended through added circuits without extra switches to achieve greater voltage gains for the EV-side sub-converter.

2. SYSTEM CONFIGURATION AND PRINCIPLE OF OPERATION

The diagram for the integrated converter is displayed in Figure 1, exemplifying the EV charging system's inclusion of EV, PV, and the grid. The topology is a three-stage charger, consisting of a grid-side bidirectional AC-DC converter, a PV-side unidirectional DC-DC converter, and an EV-side bidirectional DC-DC converter. During the charging process using grid power (G2V mode), the grid-side AC-DC converter functions in rectification mode, converting AC voltage into regulated DC voltage for the DC bus. Technical abbreviations will be defined upon first usage. In V2G, PV2G, or PV&V2G modes, when power is supplied from the EV or PV to the grid, this converter operates in inversion mode. The unidirectional POSL sub-converter on the PV-side transfers power from the PV array to the DC-bus using the voltage lift (VL) technique. It employs the Maximum power point tracking (MPPT) algorithm to maximize power output from the PV array. To control the charging and discharging of the electric vehicle (EV) battery, a bidirectional DC-DC converter with a switched quasi-Z-source is connected. This converter operates in the buck mode while in the G2V and P2V modes, and switches to the boost mode for V2G and PV&V2G modes. Furthermore, implementing a single DC-link with a capacitor and regulated DC voltage to interface the grid-side, PV-side, and EV-side converters reduces the voltage stresses on the semiconductors in this DC-DC sub-converter, resulting in enhanced efficiency.

2.1. Operating Modes

A representative operation of the converter in the different modes G2V, PV2V, V2G, PV2G, and PV&V2G, is illustrated in fig. 1. The power of each source can be seen as P_g, P_{ev}, and P_{pv} representing the power of electrical Grid, EV battery and, solar panels respectively. Fig. 2 shows the waveforms of drive signals for switches S_1, S_2, S_3 and the current of the inductors L_1, L_2 and, L_3 during different operating modes of the proposed converter.

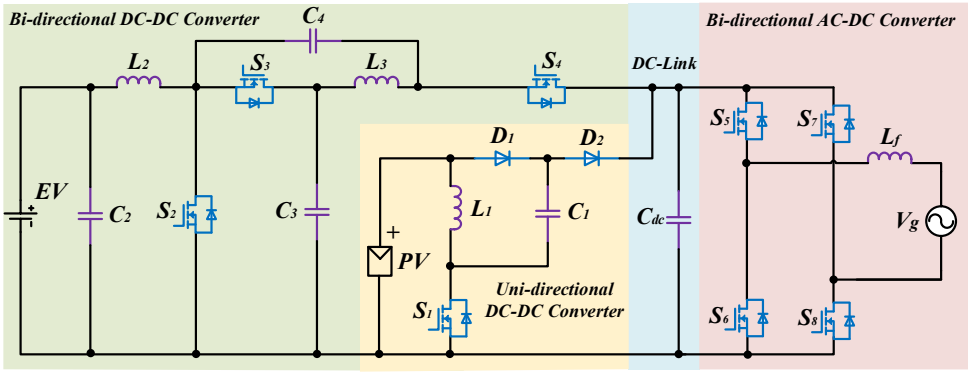

Fig. 1. the proposed converter topology for integration of PV, EV, battery, and grid.

2.1.1. G2V mode

During G2V operation period, the power flows from the electrical Grid to the EV through AC-DC bidirectional and DC-DC bidirectional converters. Therefore, the Grid side converter operates in rectification mode, while the EV-side converter works in buck mode. As can be seen in Fig. 2, in this operation mode, there is no power donating from PV therefore the MOSFET S_1 is turned off and, the MOSFETS of the EV-side sub-converter $S_2 - S_4$ are PWM controlled, as shown in Fig. 3(b). during this mode, power of the Grid and EV are equal. The G2V mode is mainly used during nights or when the PV panels are absent.

2.1.2. PV2V mode

During the next interval, the battery of EV is being charged only using PV power. Hence, the current and power of the grid Ig and $P_g$is equal to zero, and the power of the PV and EV are equal. The MPPT algorithm is utilized for the POSL converter to get the maximum power from the PV array by determining the duty cycle of the switch S_1, as can be seen in Fig. 3(a). The EV-side sub-converter operates in buck mode to charge the EV battery.

2.1.3. V2G mode

During peak demand hours for the electrical grid, the EV battery could be used as an auxiliary power source to stabilize the local grid. EV-side bidirectional sub-converter and Grid-side bidirectional sub-converter are used to deliver the power from the EV batteries to the grid. Therefore, the power of the EV and Grid are equal. As can be seen in Fig. 2, there is a 180˚ phase difference between the current, injecting to the grid, and the grid voltage, signifying that the power flow is from EV to the grid. During this mode, the switch S_1 is turned off, as shown in Fig. 3(b) and, there is no power, donated from the solar array.

2.1.4 PV2G mode

When the EV is fully charged or not connected, the power, produced by the PV array, can be delivered to the public grid through the unidirectional PV-side, and the Bidirectional Grid-side converters during this mode. As shown in Fig. 2, The PV power and grid power are equal and the current, injected into the grid, has a 180˚ phase difference with the voltage. As illustrated in Fig. 3(c), The duty cycle of switch S_1 is controlled by the MPPT algorithm, and the switches of the Bidirectional DC-DC sub-converter are turned off, which means the EV-side conversion stage is not transferring any power. Economic advantage can also be achieved, using PV2G mode during peak hours of the grid when the Feed-in Tariff (FIT) is considerably increased.

2.1.5 PV&V2G mode

During peak demand hours for Grid, both PV and EV battery sources can join together, to send the power to the electrical grid. As can be seen, the grid power in this mode is the summation of the power donated by PV and

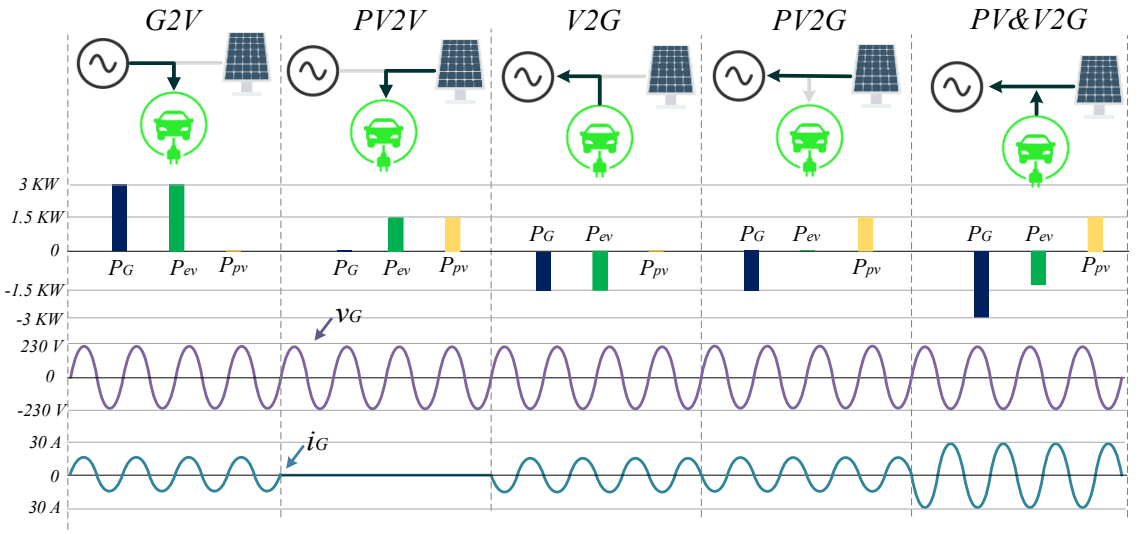

Fig. 2: Representative operation of the proposed converter for different operating modes

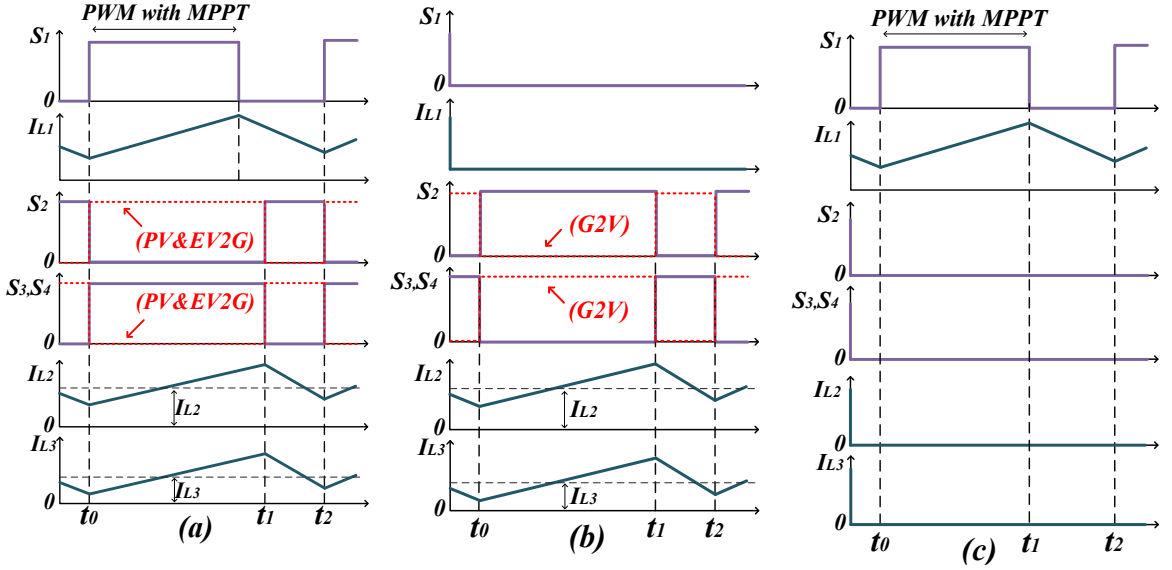

Fig. 3: Typical waveforms of the proposed converter for different operating modes

EV. As shown in Fig. 2, Since two power sources are utilized in this mode to generate the energy, The injected current and power to the grid in this mode are obviously more than before. During this mode, the EV-side DC-DC sub-converter works in boost mode, and the PV-side sub-converter is MPPT controlled to deliver the maximum power to the grid. The key waveforms of this mode are shown in Fig. 3(a)

2.1. PV-side Unidirectional DC-DC Converter

The POSL topology, which is utilized on the PV-side of the converter, works in continuous conduction mode (CCM). The circuit of this POSL sub-converter is shown in fig. 4. As can be seen, this topology consists of an inductor (L_1), capacitor (C_1), MOSFET (S_1), two freewheeling diodes (D_1 and D_2), and the filter capacitor, which is replaced by C_{DC} in the integrated topology, shown in Fig. 1. The equivalent circuits during switch on and switch off periods, are shown in Figs. 5(a) and 5(b) respectively. When the MOSFET is on, Due to the parallel connection

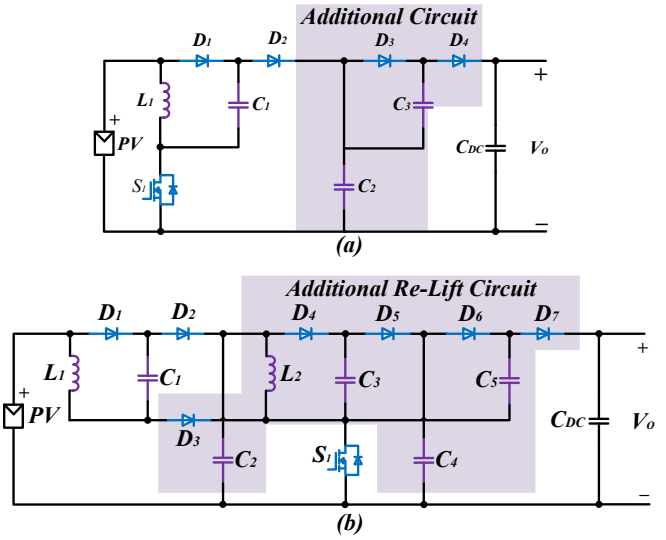

Fig. 6. Circuit diagram of POSL converter (a) with additional circuit (b) with additional re-lift circuit

between the inductor L_1 and the capacitor C_1, C_1 is charged to reach the voltage V_{pv}, and The current, flowing through inductor L_1, increases with the input voltage as can be seen in Fig. 3(a) and 3(c). When the MOSFET is turned off, The current of the I_{L1} decreases with voltage $(V_o - 2V_{pv})$, and the freewheeling diode D_1 is on. In this mode, the capacitor C_{DC} charges. The ripple of the inductor current I_{L1} can be calculated as:

$$\Delta I_{L1} = \frac{V_{pv}DT}{L_1} = \frac{V_o - 2V_{pv}(1-D)T}{L_1} \tag{1}$$

Where D is the conduction duty ratio, and T is the switching period, which is equal to $1/f$. The input current I_{in} is:

$$I_{in-on} = I_{L1-on} + I_{C1-on} \tag{2}$$

$$I_{in-off} = I_{L1-off} = I_{C1-off} \tag{3}$$

$$DTi_{C1-on} = (1 - D)Ti_{C1-on} \tag{4}$$

And the voltage gain is :

$$G = \frac{V_o}{V_{pv}} = \frac{2-D}{1-D} \tag{5}$$

Therefore, the output voltage is:

$$V_o = \frac{2-D}{1-D}V_{pv} \tag{6}$$

To achieve higher voltage gains, additional circuits can be added to the elementary topology. Fig. 6(a) and 6(b) show the topology of POSL with additional circuit and re-lift additional circuits, respectively.

Fig. 7 shows the Gain ratio of the three aforementioned converters with respect to the duty cycle of the MOSFET S_1. It is obvious that increasing the duty cycle leads to lifting the output voltage. This duty cycle is determined by the MPPT control algorithm, which will be discussed later. As can be seen, the improved gain can be achieved by adding additional circuits without additional switches. However, increasing the number of passive components can increase the size, weight, and cost of the PV-side sub-converter.

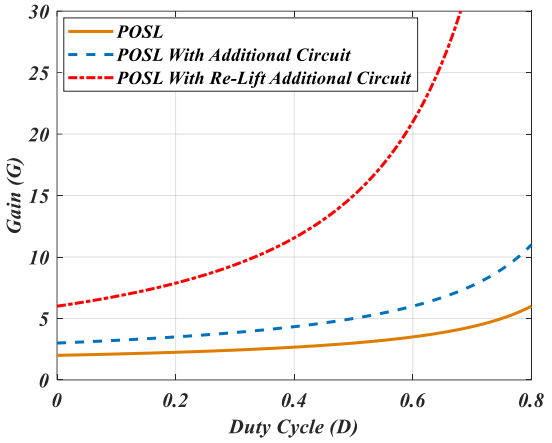

Fig. 7. Comparison of Voltage gain curves for POSL topologies

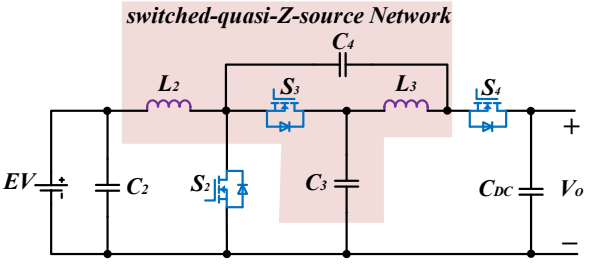

Fig. 8. Circuit diagram of Switched-Quasi-Z-Source converter

2.2. EV-side Bidirectional DC-DC Converter

The bidirectional EV-side DC-DC converter which controls the charging operation is shown in Fig. 8. This topology, consists of two switches (S_2 ,S_3), a switched-quasi-Z-source network, and two filter capacitors. this sub-converter is able to work in two modes, boost (V2G mode) and buck (G2V and PV2V mode). Operating modes of the bidirectional converter are analyzed next.

2.2.1. Operating Principle Of The Boost Mode

During this mode, energy flows from the battery of the EV to the electrical Grid. Therefore, the voltage needs to be increased to reach the voltage of the DC link. In this operating mode, the MOSFET S_1 works as a boost switch meanwhile, two other switches operate simultaneously and are complementary to the gate signal of S_2. Figs. 9(a) and 9(b), demonstrate the switching topologies and the current paths of the circuits, operating in continuous conduction mode (CCM).

Mode 1 $[t_0, t_1]$ (Fig. 9(a)): In this mode, S_2 is conducting, while S_3 and S_4 are turned off. The current flowing through switch S_1, charges the inductor L_2, and discharges the capacitor C_3. The discharge current of capacitor C_3 starts charging the inductor L_2 and the capacitor C_4. Meanwhile, the load is supplied by the DC link capacitor. For this mode, the following voltage and current equations can be derived as:

$$\begin{cases} V_{L2} = V_{EV} \\ V_{L3} = V_{C3} - V_{C4} \\ V_o = V_{CDC} \end{cases} \tag{7}$$

$$\begin{cases} I_{C3\_dboost} = -I_{L3} \\ I_{C4\_dboost} = I_{L3} \\ I_{CDC\_dboost} = -I_o \end{cases} \tag{8}$$

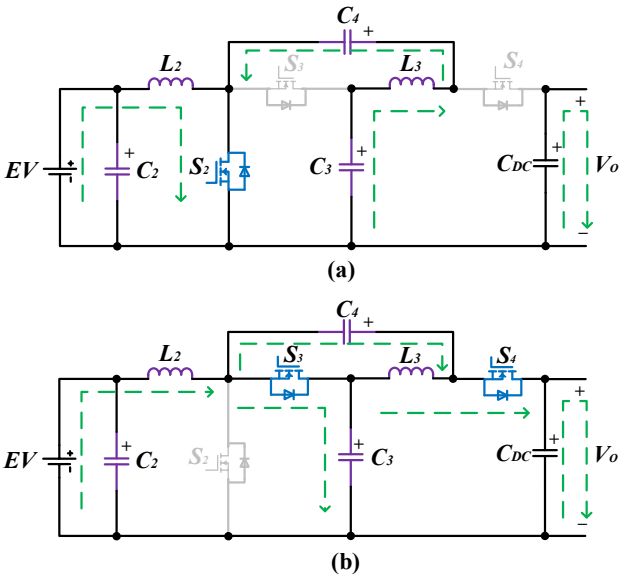

Fig. 9. Equivalent circuits of the EV-side converter during boost mode.

Mode 2 $[t_1, t_2]$ (Fig. 9(b)): In this mode, S_2 is turned off and S_3 and S_4 are turned on. The capacitor C_3, in this state, charges by the current I_{L2}, and the battery voltage, through S_3. To boost the output voltage, the capacitor C_4 and the inductor L_3 which are parallel, start charging the DC link capacitor and transfer the power to the load. For this mode, the following voltage and current equations can be derived as:

$$\begin{cases} V_{L2} = V_{EV} - V_{C3} \\ V_{L3} = V_{C3} - V_{CDC} \\ V_{CDC} = V_{C4} + V_{C3} \\ V_o = V_{CDC} \end{cases} \tag{9}$$

$$\begin{cases} I_{C3\_(1-dboost)} = I_{L2} + I_{C4\_(1-dboost)} - I_{L3} \\ I_{CDC\_(1-dboost)} = I_{L3} - I_{C4\_(1-dboost)} - I_o \end{cases} \tag{10}$$

The converter voltage gain during boost mode is calculated by applying the volt-second balance rule on inductors L_2 and L_3 with equations (7) and (9) as below:

$$G_{boost} = \frac{1 + D_{boost}}{1 - D_{boost}} \tag{11}$$

The voltage stresses on the switches S_2-S_4, according to the equivalent circuits, shown in Figs. 9(a) and 9(b), and the Kirchhoff's voltage rule, during the boost mode, is:

$$V_{S2} = V_{S3} = V_{S4} = \frac{V_{EV}}{1-D_{boost}} = \frac{V_{CDC}}{1-D_{boost}} \tag{12}$$

2.2.2. Operating Principle of the buck mode

In this mode, energy flows from the Grid or PV to the EV battery. Therefore, the converter needs to work in buck mode to provide a regulated voltage for charging operation. During this mode, the MOSFETs S_3 and S_3, work as the main switches meanwhile, the MOSFET S_2 operates simultaneously and is complementary to the gate signal of S_3 and S_4. Figs. 10(a) and 10(b) show switching topologies and the current paths of the converter in continuous conduction mode (CCM).

Mode 1 $[t_0, t_1]$ (Fig. 10(a)): In this mode S_2 is turned off and S_3 and S_4 are turned on. During this mode, input voltage and current, start charging both inductors L_2 and L_3, and the capacitor C_4 through S_3 and S_4. The capacitor C_3 discharges through S_3. For this mode following voltage equations can be derived as:

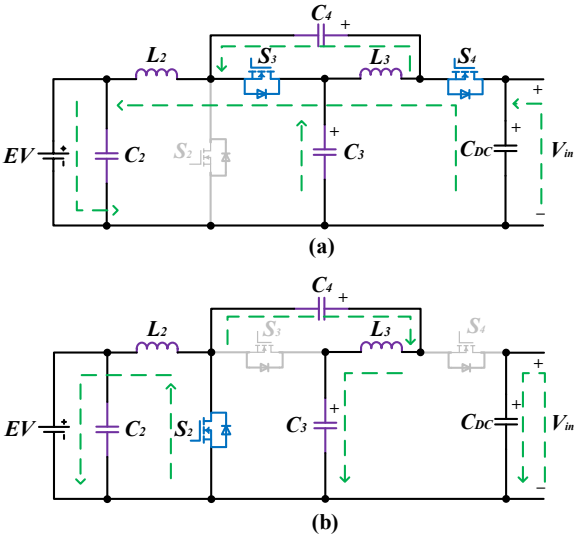

Fig. 10. Equivalent circuits of the EV-side converter during buck mode

$$\begin{cases} V_{L3} = V_{in} - V_{C3} \\ V_{L2} = V_{C3} - V_{EV} \\ V_{in} = V_{C3} + V_{C4} \\ V_{in} = V_{CDC} \end{cases} \tag{13}$$

$$\begin{cases} I_{C3\_dbuck} = I_{C4\_dbuck} - I_{L2} + I_{L3} \\ I_{C4\_dbuck} = I_{in} - I_{CDC\_dbuck} - I_{L3} \\ I_{L2} = I_{EV} + I_{C2\_dbuck} \end{cases} \tag{14}$$

Mode 2 $[t_1, t_2]$ (Fig. 10(b)): In this mode, S_2 is conducting while, S_3 and S_4 are turned off. During this state the capacitor C_4 and the inductor L_3, start to discharge and transfer their energy to the capacitor C_3 through S_2. The DC link capacitor charges by the input voltage and the inductor L_1 transfers the energy to the battery through the switch S_2. For this mode following voltage equations can be derived as:

$$\begin{cases} V_{L2} = V_{C4} - V_{C3} \\ V_{L3} = -V_{EV} \\ V_{in} = V_{CDC} \end{cases} \tag{15}$$

$$\begin{cases} I_{C3\_(1-dbuck)} = I_{L3} \\ I_{C4\_(1-dbuck)} = -I_{L3} \\ I_{CDC\_(1-dbuck)} = I_{in} \\ I_{L2} = I_{EV} + I_{C2\_(1-dbuck)} \end{cases} \tag{16}$$

The voltage gain of this converter, during boost mode, is calculated by applying the volt-second balance rule on inductors L_2 and L_3, with equations (13) and (15) as below:

$$G_{buck} = \frac{D_{buck}}{2 - D_{buck}} \tag{17}$$

The voltage stresses on the MOSFETS S_2-S_4, according to the equivalent circuits in Figs. 10(a) and 10(b) and the Kirchhoff's voltage rule, during the buck mode, is:

$$V_{S2} = V_{S3} = V_{S4} = \frac{V_{EV}}{D_{buck}} = \frac{V_{CDC}}{2 - D_{buck}} \tag{18}$$

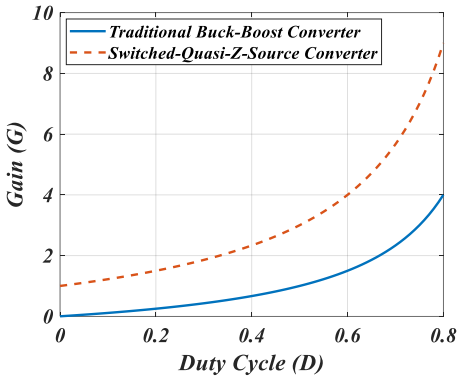

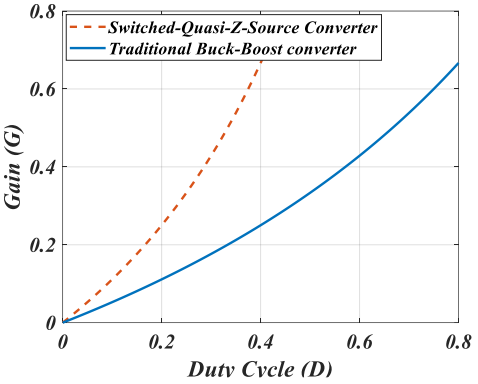

Fig. 11.(left) Comparisons of Voltage gain curves for boost mode. **Fig. 12.**(right) Comparisons of Voltage gain curves for buck mode

Figs. 11 and 12, illustrate the Gain ratio of the traditional buck-boost converter, and the Switched-Quasi-Z-Source converter, with respect to duty cycle in two modes boost and buck respectively. As can be seen, the voltage gain, can be improved in Switched-Quasi-Z-Source converter in both boost and buck mood.

2.3. Grid-side Bidirectional AC-DC Converter

The grid-side converter is connected to the grid, using a filter capacitor L_f, which is employed to limit the Total Harmonic Distortions (THD) in standards. The conversion stage consists of four switches S_5-S_6, which make a full bridge sub-converter and can be controlled by PWM pulses. The grid voltage is supposed to be sinusoidal:

$$v_s(t) = \sqrt{2}V_s Sin(\omega t) \tag{19}$$

Where $v_s(t)$ is the instantaneous grid voltage, and V_s is the Root mean square (RMS) value of this voltage. The instantaneous value of the converter voltage can be written as:

$$v_c(t) = \sqrt{2}V_c Sin(\omega t - \delta) \tag{20}$$

In which, V_c is the RMS value of v_s and δ is the phase difference between $v_c(t)$ and $v_s(t)$. The grid current can be written as: time:

$$I_s(t) = \sqrt{2}I_s Sin(\omega t - \theta) \tag{21}$$

In which, θ is the phase difference between $I_s(t)$, and $v_c(t)$. As shown in Figs. 13(a), during G2V mode, $v_s(t)$ leads $v_c(t)$, and the active power is extracted from the grid. In opposition to this, during V2G, PV2G, or PV&V2G modes, the power is delivered to the grid, and $v_c(t)$ leads $v_s(t)$, as shown in 13(b). Inasmuch as $v_c(t)$ and $v_s(t)$ have purely sinusoidal waveforms, $I_s(t)$ is similarly sinusoidal, and the direction of the reactive power flow, is determined by its phase angle θ. When this angle is negative, it implies that, the reactive power is sent from the grid to the converter. This mode is considered as inductive charging mode, as shown in Fig. 13(d). During capacitive charging mode, the grid receives the reactive power, and the phase angle θ is positive. Vector diagrams of this mode are shown in Fig. 13(c).

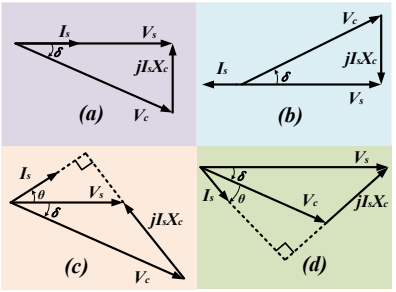

Fig. 13. the diagram of the Vectors for different operating modes of the converter

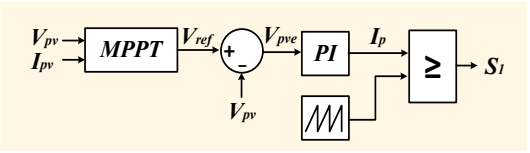

Fig. 14. Control of PV-side DC-DC sub-converter

3. CONTROL SYSTEM

3.1. Control of PV-side DC-DC Converter

Tracking the maximum electrical power in PV systems, is almost impossible, using an individual maximum power point (MPP), since the current-voltage characteristics of the PV arrays are quite nonlinear. Therefore, the PV converter is responsible for tracking the maximum power point. The duty cycle of the switch S_1, in the PV-side sub-converter in this paper is obtained from the MPPT algorithm control of the PV array. The diagram of the MPPT control is shown in Fig. 13. First, the voltage and current of the PV are processed by the MPPT algorithm, and the control signal V_{ref}, is produced, which is compared to a measured PV voltage, at K_{th} instant of tim

$$V_{pve}(k) = V_{ref}(k) - V_{pv}(k) \tag{22}$$

The reference voltage is tracked by a PI controller which generates a control signal I_p, to diminish the error of the voltage V_{epv}:

$$I_p(k) = I_p(k-1) + K_{pv}\big[V_{pve}(k) - V_{pve}(k-1)\big] + K_{iv}V_{pve}(k) \tag{23}$$

Where K_{pv} is the proportional gain, and K_{iv} is the integral gain of the PI controller. Eventually, the output signal of the PI controller is compared to a carrier signal to generate PWM pulses, and drive the MOSFET S_1.

3.2. Control of Bidirectional EV-side DC-DC Converter

The EV converter is responsible for controlling the EV charging and discharging operation. a PWM control technique is used for the bidirectional DC-DC converter, which measures the battery current, and controls the converter to regulate the charging current. As can be seen in Fig. 15, first the error signal I_{eve} is obtained from the difference between reference battery current I_{ev-ref}, and the measured battery current I_{ev}, at the K_{th} instant of time:

$$I_{eve}(k) = I_{ev-ref}(k) - I_{ev}(k) \tag{24}$$

the reference current is tracked by a PI controller, which generates a control signal I_p:

$$I_p(k) = I_p(k-1) + K_{pv}[\,I_{eve}(k) - I_{eve}(k-1)] + K_{iv}I_{eve}(k) \tag{25}$$

Then the control signal I_p, is compared to a carrier signal with a fixed switching frequency to drive S_2, S_3 and S_4 switches.

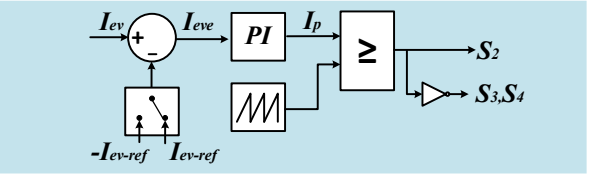

Fig. 15. Control of Bidirectional EV-side DC-DC Converter

3.3. Control of Bidirectional Grid-side AC-DC Converter

the AC-DC bidirectional controls the power balance between the DC-bus and the electrical grid. The control system of this sub-converter is illustrated in Fig. 16, in which two reference positive and negative signals are

compared with the triangular carrier waveforms. Frist, a signal error is obtained from the difference between the reference voltage V_{dc-ref}, and a measured voltage V_{dc} , at the K_{th} instant of time:

$$V_{dce}(k) = V_{dc-ref}(k) - V_{dc}(k) \tag{26}$$

Then to diminish the voltage error V_{dce}, the reference voltage V_{dc-ref} is tracked by a PI controller which produces a control signal I_p:

$$I_p(k) = I_p(k-1) + K_{pv}[\,V_{dce}(k) - V_{dce}(k-1)] + K_{iv}V_{dce}(k) \tag{27}$$

The reference current I_p, is compared with a measured Grid current I_{grid}, and the error signal I_e is sent to proportional controllers by gain K, which produces a control signal V_{cs}, to lessen the error of the current:

$$I_e(k) = I_{grid}(k) - I_p(k) \tag{28}$$

$$V_{cs} = KI_e(k) \tag{29}$$

This amplified signal is then given to a PWM generation unit with a a fixed switching frequency to generate the drive signals for the switches $S_5 - S_8$.

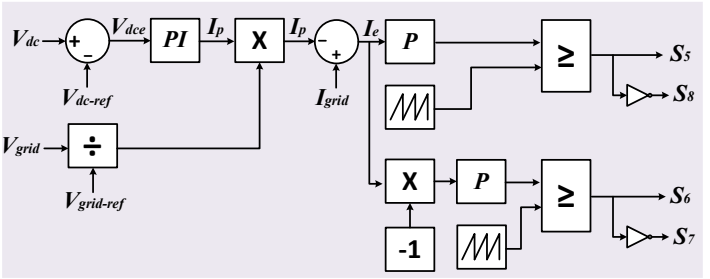

Fig. 16. Control of grid-side AC-DC sub-converter

4. SIMULATION VERIFICATION

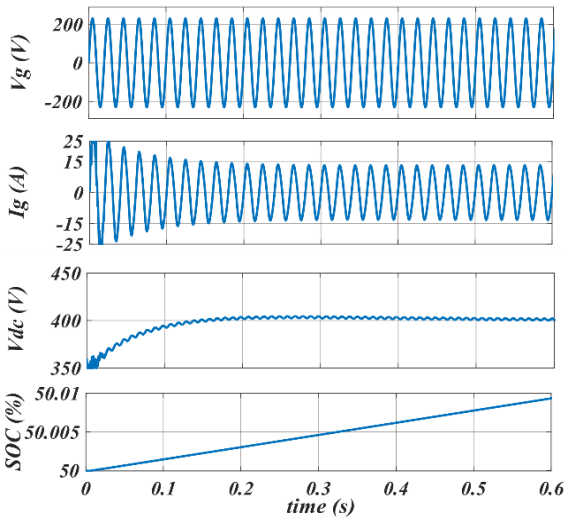

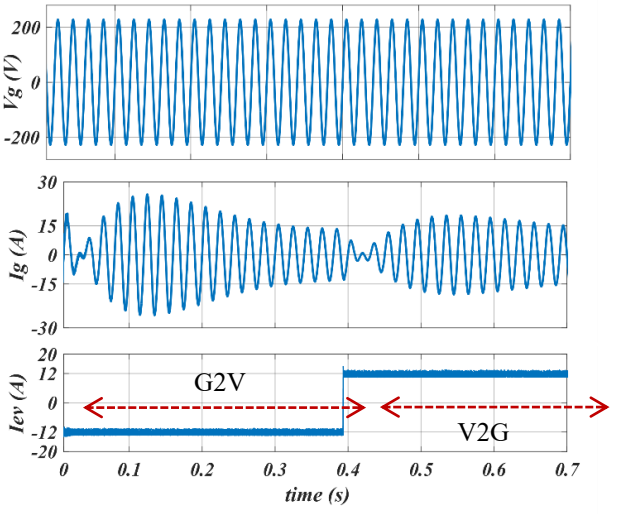

Fig. 17. (Left) Simulation output for G2V mode. **Fig. 18.** (Right) Simulation output for mode change (G2V → V2G).

The proposed multiport converter's simulated model is developed using MATLAB/Simulink and includes a bidirectional AC-DC converter on the grid-side with a 10 kHz switching frequency, a unidirectional POSL converter on the PV-side with a 100 kHz switching frequency, and a bidirectional DC-DC converter on the EV-side with a 20 kHz switching frequency. At maximum power point, the open circuit voltage of the solar array is 100 V, while the PV voltage and current are 82V and 21 A, respectively. The battery voltage is 120 volts with a charging current of 12 amps. The grid voltage is 230 volts with a frequency of 50 Hz. Figs. 16-20 display simulation results from different operating modes of the proposed integrated converter. As portrayed in Fig. 17, the

grid current has a sinusoidal waveform and is in-phase with the grid voltage in G2V mode, indicating power flow from the grid to the EV battery. Obviously, the converter maintains a voltage of 400 V for the DC-link during G2V mode, following some initial voltage transients that occur at start-up. The state of charge of the battery (SOC) begins to increase from 50%.

Fig. 18 shows the voltage grid and current waveforms, during a mode change from G2V to V2G mode. With changing the reference of the battery current in the control system, As can be seen, the battery current value, which has been -12A as the charging current, switches to 12A as discharging current. This means the EV-side bidirectional DC-DC converter changes its operating mode from buck to boost.

During V2G operation, the power delivers from the EV to the electrical grid. As can be seen in Fig. 19, there is a 180˚ phase difference between the current, injected into the electrical grid, and the voltage of the grid. This implies that, the power is transferring from the EV battery to the grid. DC-bus voltage is stabilized at 400 V, and the battery starts to discharge to send the power to the grid as SOC decreases from 50%.

Fig. 20 shows the waveforms of the grid voltage, grid current and DC-link Voltage during three operating Mode changes: V2G → PV&V2G → PV2G.

During the first time period, from 0 to 1 second, power is transferred from the battery to the grid. The DC link voltage remains stable at 400 volts, while the current to the grid is 15 amps. At 1 second, PV joins the EV battery as an auxiliary power source to elevate the power delivered to the grid. As illustrated, the injected current into the grid rises from 15 amps to 30 amps, resulting in an increase in the power contributed to the grid to enhance the electrical grid. After brief voltage fluctuations in the DC-link from 1 to 1.2 seconds, the control system stabilized the DC bus voltage at 400 volts. During the final time interval, the electric vehicle (EV) battery was disconnected from the system, and the photovoltaic (PV) system remained as the sole power source. The PV system sent power to the electrical grid through the unidirectional DC-DC converter on the PV side and the bidirectional AC-DC sub-converters on the grid side. This caused an abrupt decrease in the current injected into the Grid from 30 amps to 15 amps. Since the battery was removed as a power source from the system, there was a brief drop in the DC-link voltage, which was quickly recovered by the control system and stabilized at 400V.

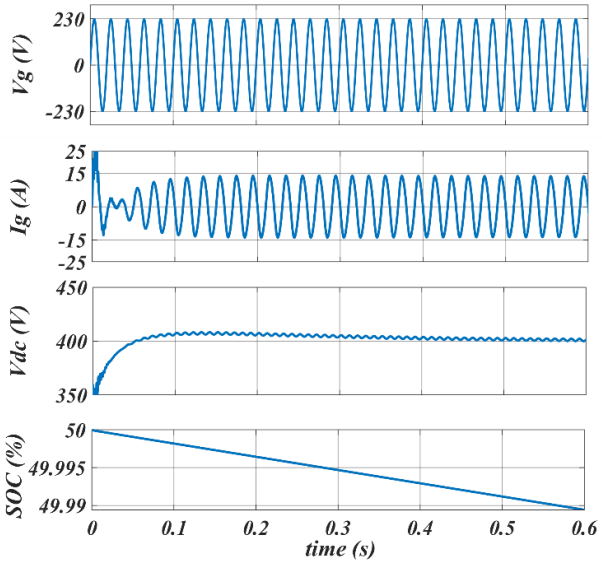

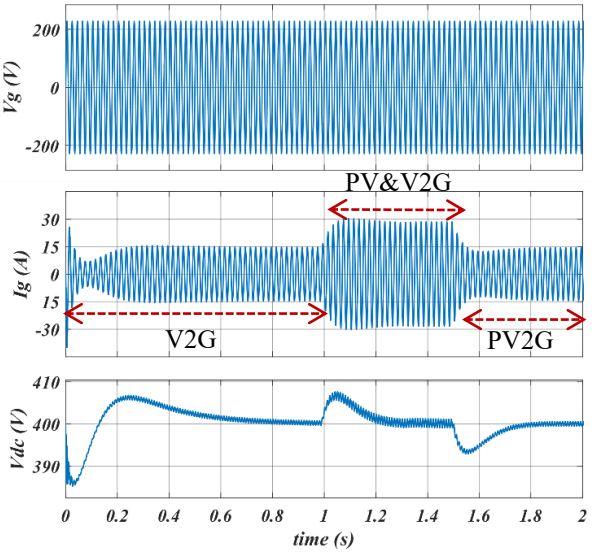

Fig. 19 (left) Simulation output for V2G mode. **Fig. 20.** (right) Simulation output for mode change (V2G → PV&V2G → PV2G).

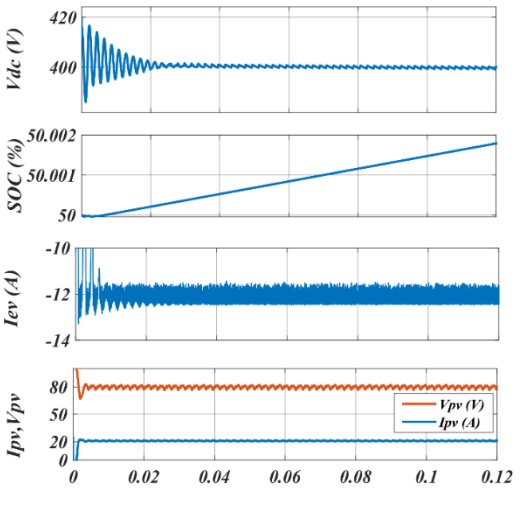

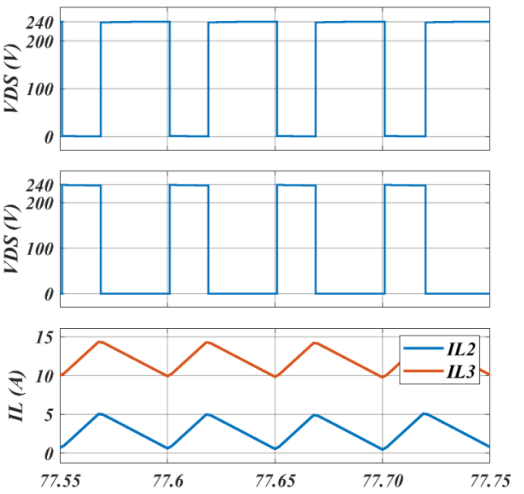

Fig. 21. (left) Simulation output for PV2V mode. **Fig. 22.** (right) waveforms of the drain-source voltage of the switches S_2, S_3, S_4 and the current of the inductors L_2, L_3

Figure 21 displays the waveforms of the DC-link voltage, battery state of charge (SOC), electric vehicle battery current, and the voltage and current of the photovoltaic (PV) array during PV2V operational mode. The control system of the PV-side DC-DC converter maintains the DC link voltage at 400 volts after a quick transient variation, as evident from the graph. Furthermore, the maximum power point tracking (MPPT) algorithm governs the PV voltage and current to remain at the specified MPPT values (80V, 21A). The battery charging current is regulated at -12A, causing the state of charge (SOC) to increase, indicating that the electric vehicle (EV) battery is being charged by the photovoltaic (PV) array's power.

Section II states that buck mode is required for the EV-side sub-converter during charging. Consequently, the MOSFETs S_3 and S_4 have duty cycles greater than that of the MOSFET S_2, as demonstrated in Fig. 22. It is noteworthy that the peak drain-source voltages for switches S_2-S_4 in the switched-quasi-Z-source converter are 240 V, slightly above half of the DC-link voltage (400 V). This lowered voltage stress can decrease MOSFET switching loss. Moreover, this converter allows for the use of power switches with low-rated voltage. The current flowing through the inductors L_1 and L_2 reaches peaks of 5A and 15A, respectively, and mimics the theoretical waveforms depicted in Figure 3. Figures 23 and 24 display the total harmonic distortion (THD) of the grid current during the G2V and V2G operating modes, respectively. The G2V mode exhibits a THD of 3.83%, whereas the V2G mode's THD is 3.79%. Both THD values are below the maximum permissible threshold of 5% specified by the IEEE standard. The low total harmonic distortion (THD) can prolong the converter's lifespan while reducing grid voltage distortions and improving power quality.

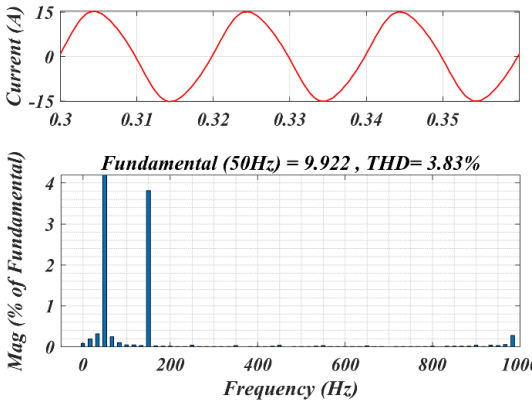

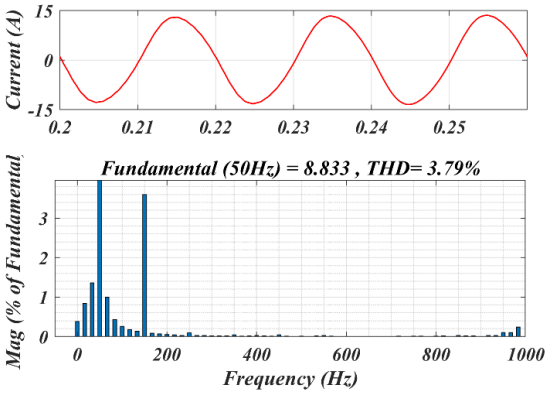

Fig. 23. (left) THD of the grid current during G2V mode **Fig. 24.** (right) THD of the grid current during G2V mode

5. CONCLUSION

A new Multiport Power Converter, integrated with PV, is proposed for grid-tied EV charging systems. The converter operates in various modes such as G2V, V2G, PV&V2G, PV2G, and PV2V. To regulate the charging operation, a bidirectional DC-DC sub-converter with switched-quasi-Z-source topology is employed in this study. The topology has reduced voltage stresses on the semiconductor switches, improving efficiency. The POSL topology is utilized for the PV-side converter and can be expanded with additional circuits to achieve a higher voltage gain. The converter also includes a bidirectional AC-DC sub-converter that transfers power to and from the grid at low current harmonics. This paper offers comprehensive analyses of the proposed converter's operational principles for the aforementioned operating modes. The precise functionality and effectiveness of the proposed converter are additionally confirmed by the simulation outcomes, utilizing MATLAB/Simulink.

CONFLICTS OF INTEREST

The authors declare no conflict of interest.

REFERENCES

[1] United States Environmental Protection Agency. (Apr. 2021). Inventory of U.S. Greenhouse Gas Emissions and Sinks. [Online]. Available: https://www.epa.gov/ghgemissions/inventory-us-greenhouse-gas-emissions-and-sinks

[2] Khan, S., Ahmad, A., Ahmad, F., Shafaati Shemami, M., Saad Alam, M., & Khateeb, S. (2018). A comprehensive review on solar powered electric vehicle charging system. Smart Science, 6(1), 54-79. https://doi.org/10.1080/23080477.2017.1419054

[3] International Energy Agency. (2021). Global EV Outlook 2021. https://doi.org/10.1787/3a394362-en

[4] Krim, Y., Sechilariu, M., & Locment, F. (2021). PV benefits assessment for PV-powered charging stations for electric vehicles. Applied Sciences, 11(9). https://doi.org/10.3390/app11094127

[5] Mobarak, M. H., Kleiman, R. N., & Bauman, J. (2021). Solar-charged electric vehicles: A comprehensive analysis of grid, driver, and environmental benefits. IEEE Transactions on Transportation Electrification, 7(2), 579-603. https://doi.org/10.1109/TTE.2020.2996363

[6] Mouli, G. R. C., Leendertse, M., Prasanth, V., Bauer, P., Silvester, S., van de Geer, S., & Zeman, M. (2016, June). Economic and CO2 emission benefits of a solar powered electric vehicle charging station for workplaces in the Netherlands. 2016 IEEE Transportation Electrification Conference and Expo (ITEC). Dearborn, MI, USA. https://doi.org/10.1109/itec.2016.7520273

[7] Yilmaz, M., & Krein, P. T. (2013). Review of the impact of vehicle-to-grid technologies on distribution systems and utility interfaces. IEEE Transactions on Power Electronics, 28(12), 5673–5689. https://doi.org/10.1109/tpel.2012.2227500

[8] Tirunagari, S., Gu, M., & Meegahapola, L. (2022). Reaping the benefits of smart electric vehicle charging and vehicle-to-grid technologies: Regulatory, policy and technical aspects. IEEE Access: Practical Innovations, Open Solutions, 10, 114657–114672. https://doi.org/10.1109/access.2022.3217525

[9] Esfahani, F., Darwish, A., & Williams, B. W. (2022). Power converter topologies for grid-tied solar photovoltaic (PV) powered electric vehicles (EVs)-A comprehensive review. Energies, 15(13). https://doi.org/10.3390/en15134648

[10] Safayatullah, M., Elrais, M. T., Ghosh, S., Rezaii, R., & Batarseh, I. (2022). A comprehensive review of power converter topologies and control methods for electric vehicle fast charging applications. IEEE Access:

Practical Innovations, Open Solutions, 10, 40753–40793. https://doi.org/10.1109/access.2022.3166935

[11] Bhatti, A. R., Salam, Z., Aziz, M. J. B. A., Yee, K. P., & Ashique, R. H. (2016). Electric vehicles charging using photovoltaic: Status and technological review. Renewable and Sustainable Energy Reviews, 54, 34–47. https://doi.org/10.1016/j.rser.2015.09.091

[12] Khan, S. A., Islam, M. R., Guo, Y., & Zhu, J. (2019). A new isolated multi-port converter with multi-directional power flow capabilities for smart electric vehicle charging stations. IEEE Transactions on Applied Superconductivity: A Publication of the IEEE Superconductivity Committee, 29(2), 1–4. https://doi.org/10.1109/tasc.2019.2895526

[13] Chandra Mouli, G. R., Schijffelen, J., van den Heuvel, M., Kardolus, M., & Bauer, P. (2019). A 10 kW solar-powered bidirectional EV charger compatible with chademo and COMBO. IEEE Transactions on Power Electronics, 34(2), 1082–1098. https://doi.org/10.1109/tpel.2018.2829211

[14] Bhattacharjee, A. K., & Batarseh, I. (2021). An interleaved boost and dual active bridge-based single-stage three-port DC–DC–AC converter with sine PWM modulation. IEEE Transactions on Industrial Electronics (1982), 68(6), 4790–4800. https://doi.org/10.1109/tie.2020.2992956

[15] Khan, O., Hredzak, B., & Fletcher, J. E. (2022, June 29). A Reconfigurable Multiport Converter for Grid Integrated Hybrid PV/EV/Battery System. 2022 IEEE 16th International Conference on Compatibility, Power Electronics, and Power Engineering (CPE-POWERENG). Birmingham, United Kingdom. https://doi.org/10.1109/cpe-powereng54966.2022.9880873

[16] Saxena, N., Hussain, I., Singh, B., & Vyas, A. L. (2018). Implementation of a grid-integrated PV-battery system for residential and electrical vehicle applications. IEEE Transactions on Industrial Electronics (1982), 65(8), 6592–6601. https://doi.org/10.1109/tie.2017.2739712

[17] Monteiro, V., Pinto, J. G., & Afonso, J. L. (2018). Experimental validation of a three-port integrated topology to interface electric vehicles and renewables with the electrical grid. IEEE Transactions on Industrial Informatics, 14(6), 2364–2374. https://doi.org/10.1109/tii.2018.2818174

[18] Verma, A., & Singh, B. (2019). Multi-Objective Reconfigurable Three-Phase Off-Board Charger for EV. IEEE Transactions on Industry Applications, 55(4), 4192–4203. https://doi.org/10.1109/tia.2019.2908950

[19] Verma, A., Singh, B., Chandra, A., & Al Haddad, K. (2020). An implementation of solar PV array based multifunctional EV charger. IEEE Transactions on Industry Applications, 1–1. https://doi.org/10.1109/tia.2020.2984742

[20] Zhang, Y., Liu, Q., Li, J., & Sumner, M. (2018). A common ground switched-quasi-Z -source bidirectional DC–DC converter with wide-voltage-gain range for EVs with hybrid energy sources. IEEE Transactions on Industrial Electronics (1982), 65(6), 5188–5200. https://doi.org/10.1109/tie.2017.2756603